

# Simulating Spin Orbit Torque Driven Switching with Ultrafast Thermal Effects

*Ashwin Rastogi*

Electrical Engineering and Computer Sciences  
University of California, Berkeley

Technical Report No. UCB/EECS-2022-103

<http://www2.eecs.berkeley.edu/Pubs/TechRpts/2022/EECS-2022-103.html>

May 13, 2022



Copyright © 2022, by the author(s).  
All rights reserved.

Permission to make digital or hard copies of all or part of this work for personal or classroom use is granted without fee provided that copies are not made or distributed for profit or commercial advantage and that copies bear this notice and the full citation on the first page. To copy otherwise, to republish, to post on servers or to redistribute to lists, requires prior specific permission.

---

**Simulating Spin Orbit Torque Driven Switching with Ultrafast Thermal Effects**  
by Ashwin Rastogi

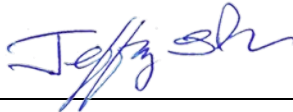
---

**Research Project**

Submitted to the Department of Electrical Engineering and Computer Sciences,  
University of California at Berkeley, in partial satisfaction of the requirements for the  
degree of **Master of Science, Plan II.**

Approval for the Report and Comprehensive Examination:

**Committee:**



---

Professor Jeffrey Bokor  
Research Advisor

May 11, 2022

---

(Date)

\* \* \* \* \*



---

Professor Sayeef Salahuddin  
Second Reader

May 13, 2022

---

(Date)

## Abstract

Simulating Spin Orbit Torque Driven Switching with Ultrafast Thermal Effects

by

Ashwin Rastogi

Master of Science in Electrical Engineering and Computer Science

University of California, Berkeley

Jeffrey Bokor

Spin-transfer torque (STT) has been used as the underlying physical mechanism in STT-RAM in industry to create fast and low-power spintronic memory devices. However, due to the geometry of STT devices, lower current densities and accordingly longer electrical pulse widths are necessary to achieve switching without device degradation. This in practice has limited STT devices to the nanosecond timescale. Spin-orbit torque (SOT) provides an alternative method of switching, i.e. writing bits, with spin currents without the limitation on current density. As a result, switching with current pulses as short as 200 ps (and 6 ps using photoconductive switches) has been demonstrated. In this work, the SOT switching mechanism on a metallic stack consisting of Cobalt magnetic thin film was simulated using the Landau-Lifshitz-Gilbert macrospin equation. The relationship between critical switching current density and other system parameters like in-plane field as well as the relationship between switching times and current density were simulated. The effects of ultrafast heating were incorporated into the simulation by solving the heat-diffusion equation and modeling saturation magnetization and anisotropy as functions of temperature. The results of the simulation are compared to experimental data and it was demonstrated that the simulation agrees well with the experiment. It is also shown that complete magnetization reversal is achievable in less than 200 ps as suggested by the simulation. These simulations enable engineers to see expected dynamics along with power consumption and response speed for a wide variety of ferromagnetic stacks without the direct need for fabrication and experimentation.

# Contents

<b>1</b>	<b>Introduction</b>	<b>1</b>
<b>2</b>	<b>Background</b>	<b>2</b>
2.1	Magnetic Order and Applications to Data Storage . . . . .	2
2.2	Macrospin Modeling with Landau-Lifshitz-Gilbert Equation . . . . .	6
2.3	Spin Hall Effect and Switching . . . . .	7
<b>3</b>	<b>Simulating Spin Orbit Torque Driven Switching</b>	<b>11</b>
3.1	LLG Dynamics in SOT . . . . .	12
3.2	Effect of Free Parameters on Simulation . . . . .	17
3.3	Ultrafast Thermal Dynamics . . . . .	19
3.4	Comparing Simulation to Experimental Data . . . . .	25
<b>4</b>	<b>Conclusion and Future Works</b>	<b>28</b>
	<b>References</b>	<b>30</b>

## Acknowledgments

Firstly, I would like to express my enormous gratitude to my research advisor Professor Jeffrey Bokor for mentoring me, for giving me the freedom to pursue enticing problems, and for guiding me throughout my undergraduate and graduate career at Berkeley. I want to further thank him for giving me an opportunity to savor another year at Berkeley by agreeing to sponsor and advise me as a Master's student. I would also like to thank Professor Sayeef Salahuddin for being the second reader for my technical report.

Much of the work that I was able to complete in the past year would not have been possible without the greatly appreciated help of graduate and postdoctoral students in the group. In particular, I would like to thank Dr. Akshay Pattabi for investing countless hours in teaching me, mentoring me, and helping me grow both as a researcher and as a person. I am grateful for his patience, camaraderie, and the many deep insights into devices he has provided me with over the last couple years.

Finally, I would like to thank my family, who have always been a source of strength and motivation. I thank my parents, Shyamala and Anu, who understood me, encouraged me, uplifted me, and supported me, for giving me the freedom to follow my dreams and find my path 10,000 miles away from home. I would also like to thank my sister, Dr. Shruti Rastogi, for being a constant source of inspiration and a great role model. Interest is something that is nurtured, and I cannot emphasize enough how impactful they have been on my interest and passion in electrical engineering, computer science, and physics. They molded me and I owe any success I may achieve to them. I know my Mom will always be proud of my achievements. I owe this degree to many people, but to her most of all.

# Chapter 1

## Introduction

Technological advances in memory have been attributed to the successful iterative down scaling of metal-oxide-semiconductor field effect transistors (MOSFETs) using complementary metal-oxide-semiconductor (CMOS) technology. While decreasing transistor sizes has led to denser chips, cheaper production per transistor, lower power consumption, and faster response, transistors cannot be perpetually shrunk. Eventually technological growth based on this premise will hit a wall due to physical limitations and signs of this are already being observed. In response, new avenues for implementing logic and memory devices are being explored using physical properties and material systems that are relatively under utilized. One such physical property is that of electrons' spin angular momentum.

Spintronics, also referred to as magnetoelectronics, is the study of how the additional intrinsic spin degree of freedom of electrons and the resulting magnetic moment can be exploited to manipulate the magnetization, in addition to the use of fundamental electronic charge in devices. New material systems involving magnetic stacks consisting of two ferromagnet layers separated by a thin insulator layer exhibit tunnel magnetoresistance (TMR) in which the resistance of the stack depends on the relative orientation of the magnetic layers' magnetization. This difference in resistance can be used to create memory devices that can be controlled using the angular momentum of spin currents — currents with electron spins polarized in a given direction. These devices would ideally require low power inputs while demonstrating fast switching, and stability. Furthermore, simulating the dynamics of these devices would enable us to identify the conditions under which they exhibit desired behavior and allow us to evaluate the effectiveness of different systems with ease. As such, simulating the ultrafast switching dynamics, specifically due to spin orbit torque, of a Cobalt stack will be the focus of this work.

# Chapter 2

## Background

### 2.1 Magnetic Order and Applications to Data Storage

Materials are generally said to be magnetic if they sustain magnetic order in the absence of an external field. On an atomic scale, magnetic properties arise from the angular momentum (a kind of momentum that comes from rotational motion about some axis) of charges, which is dominated by that of electrons. This angular momentum leads to the formation of magnetic dipole moments  $\vec{m}$ , or magnetic moments for short, where the moment is proportional to the magnitude of angular momentum. Electrons poses two kinds of angular momentum that contribute to the formation of their magnetic dipoles.

The first is orbital angular momenta which, as the name suggests, arises from the rotation of the electron about the nucleus. The orbital contribution is modeled as a conductive coil which has moment  $\vec{m}_{L,i} = I\vec{A}$ , where  $I$  is the effective current due to the moving electron and  $\vec{A}$  is the area of the loop that the electron completes with direction normal to the surface according to a right hand rule. The total orbital dipole moment of the atom  $\vec{m}_L$  is calculated by summing the individual orbital moments of all the electrons.

The second contribution to angular momentum is that of spin. The spin of an electron is a quantum mechanical angular momenta, i.e. it has no classical counterpart, and is an intrinsic property of the elementary particle. Nonetheless, for qualitative purposes the spin of an electron can be visualized as the electrons rotation about a central axis. Electron's spins are quantized along an axis to be either "up" or "down", representing the direction being parallel or antiparallel to the axis of measurement. The resulting spin magnetic moment is given by  $\vec{m}_{S,i} = \gamma\vec{S}$ , where  $\gamma$  is the gyromagnetic ratio of the electron (the ratio of its magnetic moment to angular momentum) and  $\vec{S}$  is its spin. The total contribution of the spin angular momentum to the atom's magnetic moment  $\vec{m}_S$  is derived by summing over the individual spin moments of all the electrons.

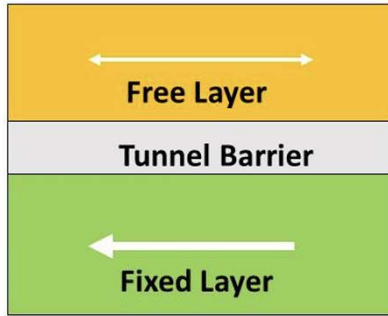


Finally, the total magnetic moment of the atom is  $\vec{m} = \vec{m}_L + \vec{m}_S$ . However, the orbital moment in magnetic materials is much smaller than and is dominated by the spin moment, and the largest contribution to the spin magnetic moment arises from unpaired electrons in the outermost energy shell. Consequently, the exchange and interaction between these unpaired outershell electrons often dictate the behavior of the magnetic material. Based on the interaction and arrangement of moments, the magnetic materials can be classified into different categories of magnets. Magnetic materials in which neighboring moments tend to align in a parallel fashion to one another are called ferromagnets. Thin films of Co/Pt are examples of ferromagnets and are the subject of this work. Another important magnetic classification is that of ferrimagnets in which neighboring moments align in an anti-parallel fashion to one another but have different magnitudes because of which a net magnetic order exists.

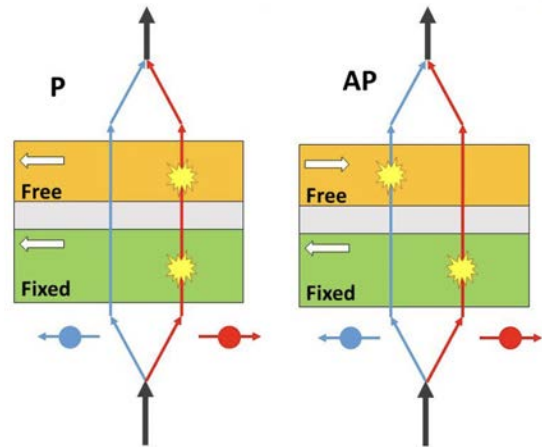
The magnetization  $\vec{M}$  of the material is the net density of magnetic moments, i.e.  $\vec{M} = \frac{1}{V} \sum \vec{m}$ . Magnetic materials often have preferential directions or axes along which it is energetically favorable for the magnetization to align. This property of magnets is referred to as magnetic anisotropy. The axis along which the magnetization prefers to align with is called the easy axis and accordingly the axis along which it is energetically unfavorable to align with is called the hard axis. The magnetic materials discussed in this work display perpendicular magnetic anisotropy in which the easy axis is orthogonal to the plane of the sample. Magnetic anisotropy is a very useful phenomena as magnetic thin films can be engineered to have uniaxial anisotropy in which the material has only one easy axis and strongly prefers to be either parallel or antiparallel to this axis. The preference of only two states, along with the bi-stability due to coercivity, lends itself to store binary bits where parallel alignment indicates a 1 and antiparallel alignment indicates a 0, vice-versa. Furthermore, tunnel magnetoresistance (TMR) of magnetic tunnel junctions (MTJ) can be used to identify the corresponding bit value.

An MTJ consists of a magnetic free layer that can be manipulated and a magnetic fixed layer that remains unchanged, separated by an insulator, often MgO. A current is then passed through the structure and resistances are measured. The structure of an MTJ and the parallel (P) and antiparallel (AP) orientations can be seen in Figure 2.1. As can be seen in Figure 2.1, an asymmetry exists between the density of occupied spin up and spin down states of conduction electrons in the two layers which results with a difference in scattering rates for the two spins. In the parallel orientation of the free and fixed layers, the spin down electrons are scattered greatly due to the large density of empty minority 3d electron states in the fixed layer, while electrons in the opposite orientation are not scattered significantly. As such, at least one orientation faces relatively low resistance through the junction. On the other hand, in the antiparallel case, both orientations are scattered greatly by either the fixed, or the free layer. As a result, the resistance of the antiparallel case is much greater than that of the parallel case. Details of scattering, MTJs, and TMR are not discussed here but can be found in Ref [4]. This difference in resistance along with the persistence

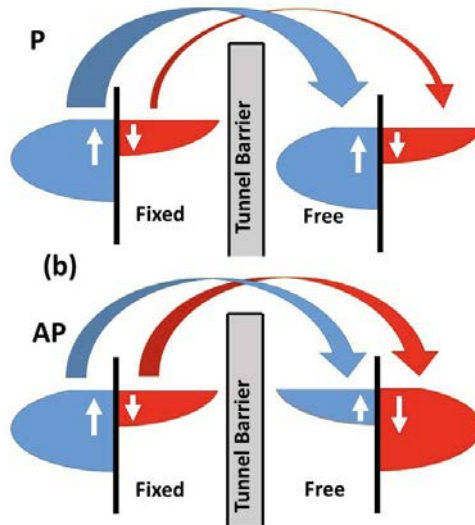
of bit storage due to magnetic anisotropy enable ferromagnets to be read. Several methods of writing data are being pursued, one of which is spin orbit torque driven switching of the ferromagnetic free layer and will be discussed in more detail in the following sections.



(a) Magnetic Tunnel Junction (MTJ) schematic. The free layer is a ferromagnet and its alignment is used to store/represent bits.



(b) Schematic for TMR with the parallel (left) and antiparallel (right) orientations. The collisions represent scattering due to the relative alignment of the magnets.



(c) Density of states schematic for the occupied spin up and spin down conduction electrons in the parallel and antiparallel MTJ orientations.

Figure 2.1: MTJ can be used with TMR to identify whether the free and fixed layers are in a parallel or antiparallel orientation due to significantly different resistances arising from scattering of spins in the magnetic layers. (Figure from Ref [12])

## 2.2 Macrospin Modeling with Landau-Lifshitz-Gilbert Equation

In general, the magnetization of ferromagnets can vary based on position but its magnitude at each point is given by the saturation magnetization  $M_s$ . When in the presence of an external magnetic field, the individual moments experience a precessional torque about the external field and a damping torque that converges the magnetization to align with the external field. As aforementioned, neighboring moments in ferromagnets tend to align parallel to each other. As a result, in the presence of an external field, one model for the magnetization of the ferromagnet is that of a single moment  $\vec{M}$  independent of position.

More generally, the time-resolved dynamics of the magnetization can be determined by examining the energy of the system. In the presence of an external field  $\vec{H}$ , the Hamiltonian is

$$H_s = \gamma \vec{S} \cdot \vec{B}, \quad \vec{B}(t) = \mu_0 \vec{H}(t) \quad (2.1)$$

where  $\gamma$  is the gyromagnetic ratio,  $\mu_0$  is the permeability of free space,  $\vec{H}(t)$  and  $\vec{B}(t)$  are the external field, and  $\vec{S}$  is the spin operator. The Schrodinger equation can easily be reduced using angular momentum commutation relations to show that the expectation value of the spin operator satisfies

$$\frac{d}{dt} \langle \vec{S} \rangle = -\gamma \langle \vec{S} \rangle \times \vec{B}(t) \quad (2.2)$$

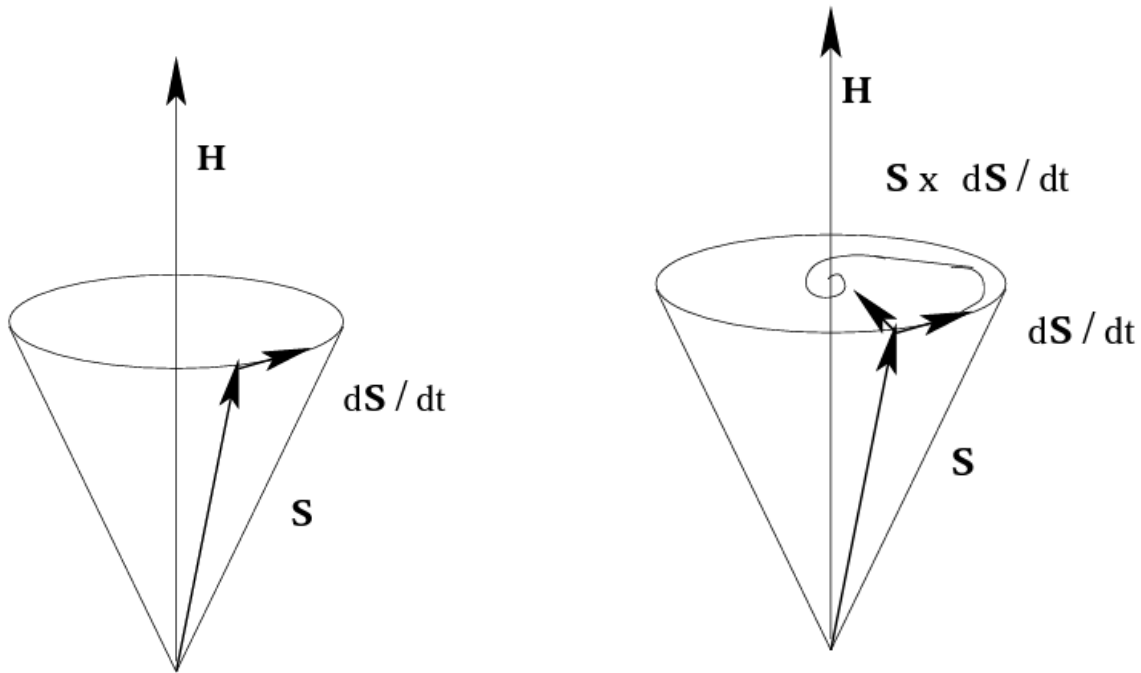
As previously explained, majority of the contribution to magnetization comes from spin angular momentum, given by  $\vec{M}_i = \gamma \vec{S}_i$ . Hence, the total magnetization can be derived using the expectation value of the spin operator on the ensemble of electrons,  $\vec{M} = \gamma \langle \vec{S} \rangle$ . The magnetization dynamics can then be derived by combining the spin-magnetization relation with Eq 2.1 and Eq 2.2 to get,

$$\frac{d\vec{M}}{dt} = -\gamma \mu_0 [\vec{M} \times \vec{H}(t)] \quad (2.3)$$

The rate of change of magnetization according to Eq 2.3 is always perpendicular to both the magnetization and the external field. As can be seen in Figure 2.2, the magnetization will precess about the external field while remaining constant in magnitude and the radius of precession remains unchanged. However, experimentally determined hysteresis loops of ferromagnets demonstrate that magnetization saturates in the presence of a strong enough external field and aligns in the same direction. Furthermore, since the Hamiltonian is the scalar product of magnetization and the external field, in order for energy to be minimized the magnetization must align with the external field. In order to account for this, a phenomenological damping torque term can be deduced,

$$\frac{d\vec{M}}{dt} = -\gamma \mu_0 [\vec{M} \times \vec{H}(t)] + \frac{\alpha}{M_s} [\vec{M} \times \frac{d\vec{M}}{dt}] \quad (2.4)$$

where  $\alpha$  is known as the Gilbert damping parameter, and  $M_s$  is the saturation magnetization and is used to gain the unit vector in  $\vec{M}$  direction. The Gilbert damping parameter is experimentally determined usually using optical fits. This completes the Landau-Lifshitz-Gilbert equation. The effect of this damping term is to produce a radially inward torque that shrinks the radius of precession and brings the magnetization to point along the external field with magnitude  $M_s$ .



(a) Effect of the field-like torque that results with precession about the external field. Here  $\vec{S}$  is proportional to  $\vec{M}$

(b) Effect of the damping torque that brings the magnetization to be along the external field.

Figure 2.2: The resulting dynamics of magnetization in the presence of an external field according to the LLG equation. (Figure from Ref [7])

## 2.3 Spin Hall Effect and Switching

As mentioned in the introduction, spintronics exploits the magnetic moments of electrons due to their intrinsic spin in addition to their charge in memory devices. From section 2.1 and 2.2, it can then be established that the magnetic moments of electrons can be used to generate an external field and influence the magnetization of an MTJ's free layer. However, due to the small size of electron's magnetic moments relative to the coercivity of the ferromagnetic free layer, a continuous current of spin polarized electrons, referred to as a spin

current, is often used to exert a torque according to the LLG equation. One such method of writing magnetic bits with spin currents is spin-transfer torque (STT). STT has been increasingly implemented in industrial spintronic devices over the last couple decades [13] [11]. In STT devices when in an antiparallel orientation, a current is passed through a structure like that in Figure 2.1 (a) first passing through the fixed layer, the tunnel barrier, and then out of the free layer. As the current enters the fixed layer, it has no special spin polarization. However, due to the magnetization of the fixed layer, the mobility of electrons with spin parallel to the fixed layer's magnetization is significantly greater than that of electrons with spin antiparallel to the magnetization. As a result, the current injected into the free layer is spin polarized along the magnetization of the fixed layer and influences the magnetization of the free layer to reverse. In the case of parallel orientation, a current is passed through the free layer first and the free layer behaves as a spin filter with the spins reflected by the tunnel barrier being in opposite direction as that of the previous case. The reflected spins accordingly create a reversing torque on the free layer. This STT switching mechanism is implemented in spin-transfer torque based magnetic random access memory (STT-RAM).

While STT devices are more energy efficient than field-based devices, they typically require high current densities for switching. These high current densities bombard the tunnel barrier which leads to degradation and eventually device failure. Hence, lower current densities with longer pulse widths would be needed for switching which is one of the reasons why STT devices are in practice limited to nanosecond timescales [14]. An alternative approach is to use spin-orbit torque (SOT) in which the spin Hall effect is used to inject spins into a ferromagnet.

In the classical Hall effect, moving charges in a current carrying wire experience a Lorentz force in the vicinity of an external magnetic field. This force causes the appearance of charge accumulation on lateral surfaces of the conductor with opposite boundaries having opposite charges. Analogously, in the spin Hall effect, spin dependent interaction of electrons with the conductor causes the appearance of spin accumulation on the conductor surface with opposite boundaries having opposite spins. Unlike the classical Hall effect, however, the spin Hall effect is a completely spin based phenomenon and does not require any external field. In place of the external field, there are two physical mechanisms that give rise to the spin Hall effect. The extrinsic mechanism consists of Mott scattering in which electrons with opposite spins scatter asymmetrically in collisions with impurities. The other intrinsic mechanism is that the electrons' spin dependent spin-orbit interactions cause distortions in its trajectory that lead to opposite spins scattering in opposite directions.

The spin Hall effect, when the conductor is in contact with a ferromagnet, essentially leads to a diffusion of polarized spins into the ferromagnet. The rate at which the spin polarized electrons are injected into the ferromagnet is the spin current. The magnitude of the spin current is proportional to the magnitude of the charge current and the constant of proportionality is called the spin Hall angle. The spin Hall angle of a material quantifies the conversion efficiency between charge current and spin current. The generated spin current

is given by,

$$\vec{J}_s = \frac{\hbar}{2q_e} \theta_{SH} (\vec{J}_e \times \sigma) \quad (2.5)$$

where  $\vec{J}_s$  is the spin current,  $\vec{J}_e$  is the charge current,  $\hbar$  is the reduced Planck's constant,  $q_e$  is the elementary charge of an electron, and  $\sigma$  is a unit vector pointing in the direction of spin polarization. A schematic representation of the spin Hall effect can be found in Figure 2.3 below.

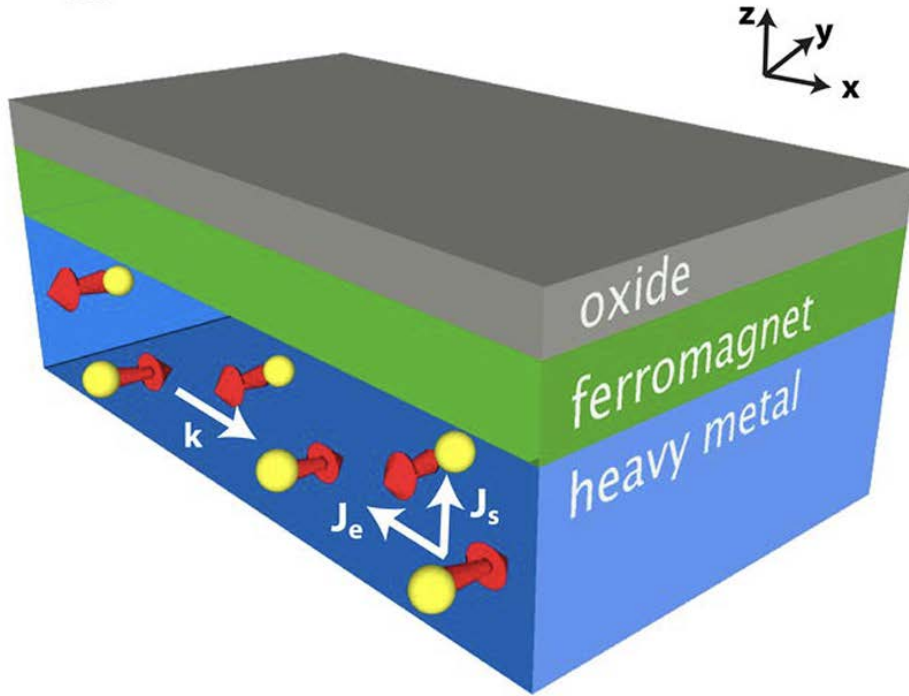


Figure 2.3: Schematic representation of the spin Hall effect. Here, the charge current is flowing in the  $-x$  direction, i.e. the electrons are moving in  $x$  direction with velocity proportional to  $k$ . The spin "up" and spin "down" electrons are separated to the top and bottom of the conductor according to the spin Hall effect. The diagram also shows the formation of a spin current  $J_s$  traveling in the  $z$  direction at the ferromagnet interface. (Figure from [3])

The generated spin current of course carries angular momentum and hence magnetic moments that, according to the LLG dynamics equation, can be used to manipulate the magnetization of the ferromagnet. Because of the geometry of SOT devices, the spin current does not pass through a tunnel barrier. Consequently, larger current densities can be used which allow for faster switching. In fact, the simulations in this work, along with the experimental data it is compared to, demonstrate SOT switching in timescales as short as 200 ps [5].

Majority of this work will be based on SOT switching and more details about magnetization reversal will provided in section 3.



## Chapter 3

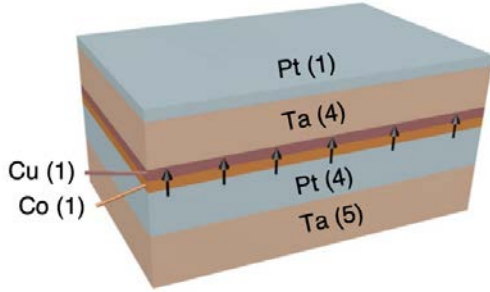
# Simulating Spin Orbit Torque Driven Switching

As previously explained, ferromagnets like Co/Pt contain a non-zero net magnetic order in which neighboring moments tend to align in a parallel fashion relative to each other. These segments of aligned moments are called domains. In the presence of an external magnetic field, these domains align and the overall magnetization of the material, i.e. the density of magnetic moments, experiences a field-like torque that causes the magnetization to undergo gyroscopic precession about the external field direction. The magnetization also experiences a damping-like torque that causes the precession radius to shrink, i.e. the magnetization eventually aligns with the external magnetic field. This alignment feature of moments in ferromagnets allows us to use simplifying macrospin models like the LLG equation in which the magnetization resulting from individual magnetic moments can be treated as a single vector, independent of position.

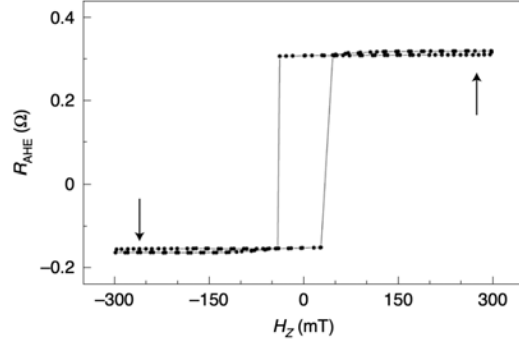
In discussing the orientation of the pertinent fields in SOT driven switching, the out-of-plane field of the ferromagnet will be taken to be along the  $z$  direction, the external magnetic field will be confined to the  $xz$  plane, and the magnetic moment due to the spin current will be either parallel or anti-parallel to the  $y$  direction, which will be referred to as positive and negative current, respectively. The material's magnetization may vary in any direction through the switching process.

All of the simulations in this work are based on a hetero-structure comprising of a 1 nm magnetic Cobalt thin film that is injected with a 6 ps Full Width Half Maximum (FWHM) electrical pulse generated via photoconductive switches [1]. The structure of the magnetic stack, Ta(5 nm)/Pt(4 nm)/Co(1 nm)/Cu(1 nm)/Ta(4 nm)/Pt(1 nm) on silicon dioxide substrate, and the Co layer's perpendicular magnetic anisotropy can be seen in Figure 3.1.

In this structure, the 1 nm thickness of the Co thin film causes the resistivity across Co to be relatively large compared to the 4 nm layers of Ta and Pt. As a result, much like in



(a) Magnetic thin film structure with spin Hall angle direction denoted. Numbers in parenthesis are thickness in nm.



(b) Anomalous Hall resistance as a function of out-of-plane field indicating coercivity of the magnetic stack.

Figure 3.1: Magnetic film structure and coercivity used in simulation

the case of parallel resistors with one having significantly higher resistance than the other, majority of the current through the sample is expected to pass through the Ta and Pt layers. Ta and Pt have opposite spin Hall angle signs which, along with Co's large spin diffusion length, enhances the torques that the spin current applies on Co's magnetization [18]. The simulation, detailed in the following section, accounts for switching using the torques of both the external field and the spin current.

### 3.1 LLG Dynamics in SOT

The LLG differential equation for a ferromagnet in an external field can be extended by linearity to include the effect of the spin current. The torques on the magnetization due to the spin current's magnetic moment is modulated by the field-like spin Hall angle and the anti-damping spin Hall angle. The modified model has the following form:

$$\frac{d\vec{M}}{dt} = -\gamma\mu_0(\vec{M} \times \vec{H}_{eff}) + \frac{\alpha}{M_s}(\vec{M} \times \frac{d\vec{M}}{dt}) + \theta_{SH}^{FL}C_s(\vec{M} \times \vec{\sigma}) - \theta_{SH}^{DL}\frac{C_s}{M_s}(\vec{M} \times (\vec{M} \times \vec{\sigma})) \quad (3.1)$$

where  $C_s = \frac{\mu_B J_C}{q_e d_0 M_s}$

In the first two terms detailing the interaction of the ferromagnet with the external field,  $\mu_0$  is the permeability of free space,  $\gamma$  is the gyromagnetic ratio of electrons (also known as the magnetogyric ratio),  $\vec{M}$  is the magnetization of Co,  $\vec{H}_{eff}$  is the effective external field which

consists of the external field, demagnetization field, and magnetocrystalline anisotropy,  $\alpha$  is Gilbert damping parameter, and  $M_s$  is the saturation magnetization. In the last two terms that incorporate the action of the spin currents,  $\theta_{SH}^{FL}$  and  $\theta_{SH}^{DL}$  are the field-like and anti-damping spin Hall angles, respectively, and  $\vec{\sigma}$  is the unit vector that points in the same direction as the spin current's magnetic moment while the magnitude of the torque's effect is absorbed into the  $C_s$  variable. For  $C_s$ ,  $\mu_B$  is the Bohr magneton,  $J_C$  is the current density at that moment in time,  $q_e$  is the elementary charge of an electron, and  $d_0$  is the thickness of Co.

As explained above,  $\vec{H}_{eff} = \vec{H}_{ext} + \vec{H}_{ani} + \vec{H}_{demag}$ . The thin film shape anisotropy demagnetization field in the z-direction is given by  $\vec{H}_{demag} = -M_s \vec{m}_z$  where  $\vec{m}_z$  is the component of the normalized magnetization in the z-direction. The anisotropy component is given by  $\vec{H}_{ani} = \frac{2K_z m_z}{\mu_0 M_s} \hat{z}$  where  $K_z$  is the material's perpendicular anisotropy constant. Together, the effective external field has the form:

$$\vec{H}_{eff} = \begin{bmatrix} H_x \\ H_y \\ H_z + \left( \frac{2K_z}{\mu_0 M_s} - M_s \right) m_z \end{bmatrix} \quad (3.2)$$

All terms in Eq 3.1 have now been defined explicitly and the values for the terms used by the simulation can be found in Table 3.1. In this work, parameters like field-like and anti-damping spin Hall angles as well as the Gilbert damping parameter are free variables that are fit to experimental data. The effect of varying these hyperparameters will be discussed in section 3.2, however, for the majority of the simulations these values are taken to be  $\theta_{SH}^{FL} = 0.05$ ,  $\theta_{SH}^{DL} = 0.3$ , and  $\alpha = 0.23$  [1].

Table 3.1: Simulation Parameter Values

Saturation magnetization	$M_s$	$10^6$	$\text{Am}^{-1}$
Anisotropy Constant	$K_z$	$10^6$	$\text{Jm}^{-3}$
Gilbert damping	$\alpha$	0.23	–
Thickness of magnetic layer	$d_0$	1	nm
Thickness of full stack	$d$	16	nm
Field-like spin Hall angle	$\theta_{SH}^{FL}$	0.05	–
Damping-like spin Hall angle	$\theta_{SH}^{DL}$	0.2	–
Current density	$J_C$	variable	$\text{Am}^{-2}$

To find the initial or equilibrium state of the magnetization before the current pulse, i.e. the state with lowest free energy  $\vec{M}(t < 0) = \vec{M}_0$ ,  $\frac{d\vec{M}}{dt}$  is set to 0, and  $\vec{M}$  is set to be along any arbitrary direction not parallel or anti-parallel to  $\vec{H}_{eff}$  with magnitude  $M_s$ . The LLG equation is then solved in the presence of the external field with no spin current. The dynamics

of the components of magnetization  $\vec{M}(t) = M_s [m_x \ m_y \ m_z]$  are shown below in Figure 3.2. Here, an in-plane field of 160 mT and an out-of-plane field of 75 mT was used.

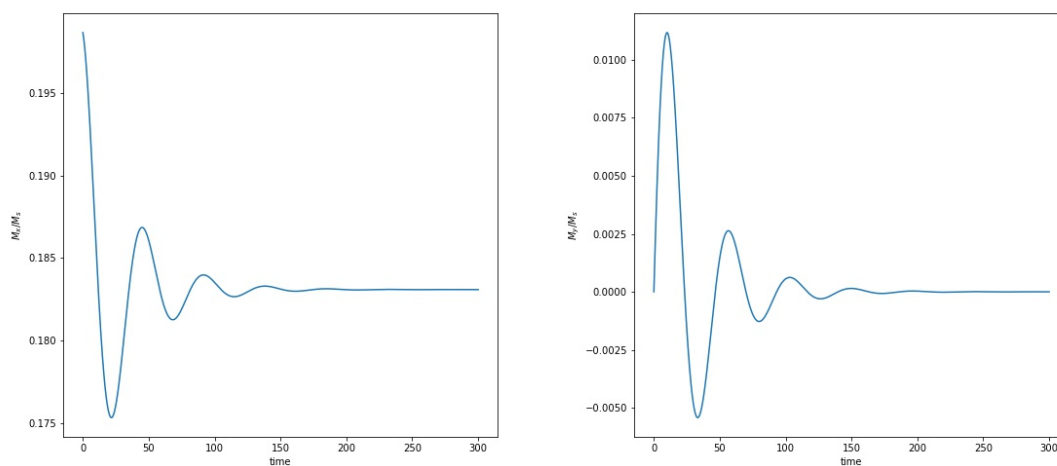
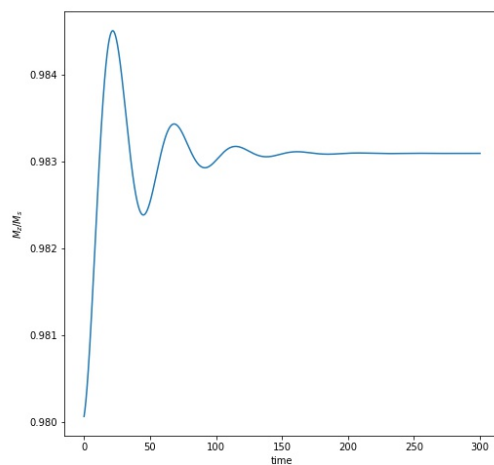
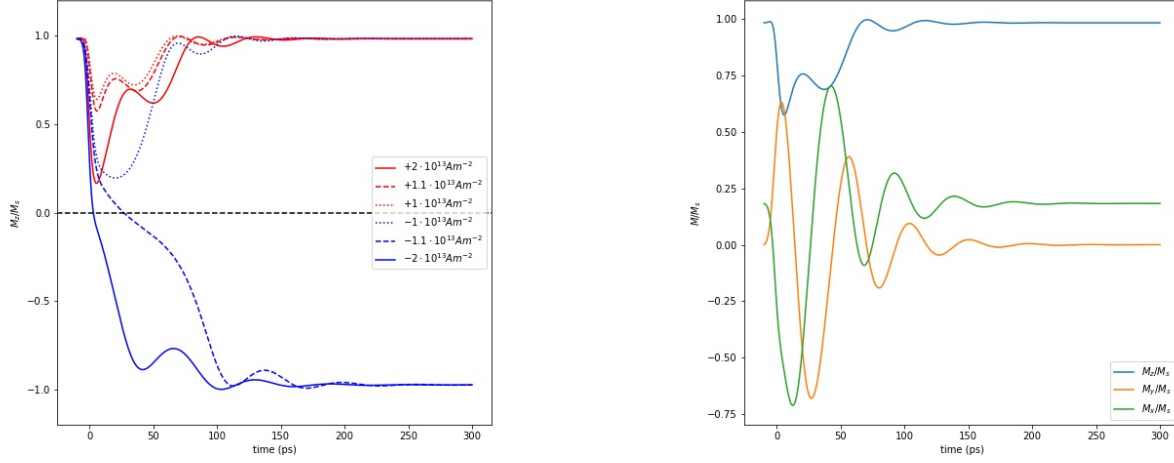
(a) Magnetization in the  $x$  direction(b) Magnetization in the  $y$  direction(c) Magnetization in the  $z$  direction

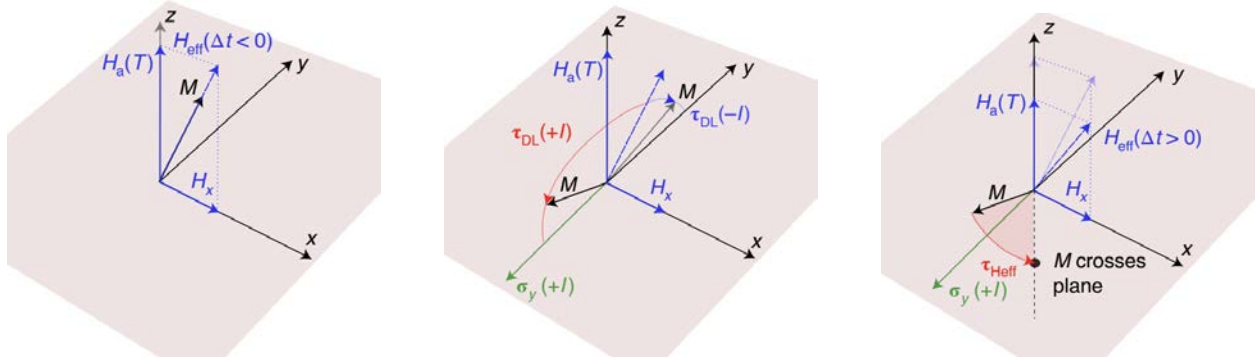
Figure 3.2: Magnetization dynamics of Co with only an external field to calculate initial equilibrium orientation.

$\vec{M}_0$  will align in the same direction as the effective external field, which has only an  $x$  and  $z$  component, provided that  $H_z$  is larger than the coercivity of Co shown in Figure 3.1 (b).



(a) Dynamics of normalized out-of-plane magnetization for different currents and spin polarizations

(b) Dynamics of all three components of normalized magnetization for threshold current and positive spin polarization



(c)  $\Delta t < 0$ , i.e. equilibrium position

(d)  $0 < \Delta t < 6$  ps, i.e. effect of spin's damping-like torque

(e)  $\Delta t > 6$  ps, i.e. precession about  $\vec{H}_{\text{eff}}$

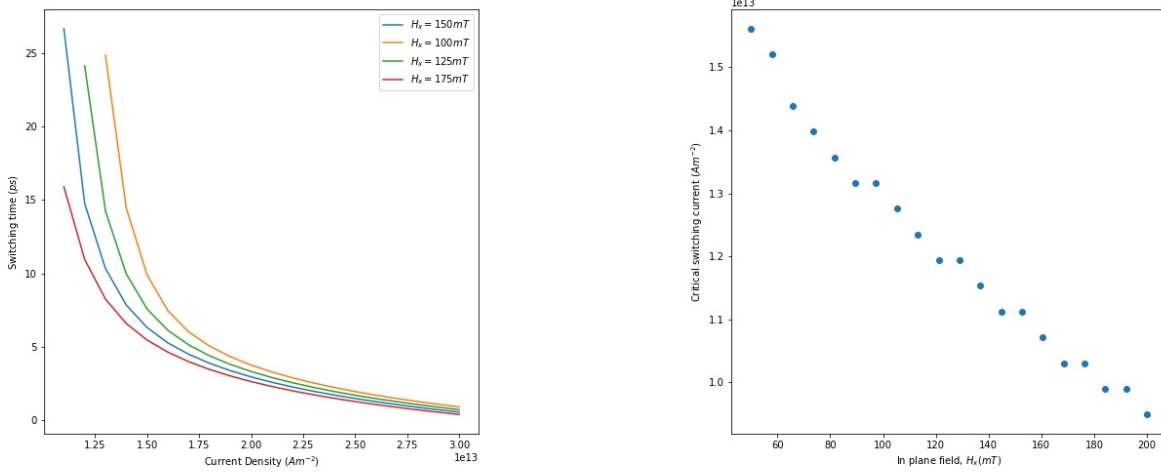
Figure 3.3: Dynamics of Co's magnetization with injected spins from a  $1.1 \times 10^{13} \text{Am}^{-2}$  current along with  $H_x = 150$  mT and  $H_z = 75$  mT

The LLG equation is solved using the finite differences method in both  $t < 0$  and  $t > 0$  cases where the magnetization is evolved forward in time using increments of  $\Delta t = 1$  fs. It was verified that the solution was stable and results were unchanged with smaller increments. The solution to the LLG equation for SOT driven switching is provided in Figure 3.3 for both positive and negative current along with varied current densities.

As can be seen in the above plots, the negative current acts as a switching current whereas

the positive current causes precession but does not result with any reversal. The damping-like torque  $\vec{\tau}_{DL} \sim \vec{M} \times \vec{M} \times \vec{\sigma}$  brings the magnetization towards the  $xy$  plane as soon as the current arrives. The magnetization begins to precess around the effective external field and the direction of the in-plane field and the direction of the injected spins determines whether reversal will occur. The two orientations would have a  $180^\circ$  phase difference when aligned with the  $y$  axis as can be seen in Figure 3.3 (d). As a result, the in-plane field  $H_x$  would create a reversing torque on the magnetization in the case of negative current and a correcting or restoring torque in the case of positive current according to Eq 3.1.

For SOT switching without considering any ultrafast thermal effects, the simulation suggests that the critical switching current density for the stack is close to  $1.1 \times 10^{13} \text{Am}^{-2}$  with the associated switching time of  $\sim 25$  ps for an in-plane field of  $H_x = 150$  mT. The switching time dramatically decreases as current density increases as can be seen in Figure 3.4 below. The figure also depicts the effect of the in-plane field on the switching times and critical threshold current. As the in-plane field increases, the magnitude of the reversing torque is larger and the required torque from the injected spins for switching is lower. Accordingly, for the same current densities, the switching time is faster at higher in-plane fields. The magnetization of the ferromagnet returns to 80% of  $M_s$  in around 50 ps with either a positive and negative current and the oscillations damp significantly past 100 ps delay and stabilize around 120 ps. A recurring feature of the out-of-plane magnetization dynamics is the two significant dips in magnitude when a positive current is applied as can be seen with the red curves in Figure 3.3. These dips occur due to the precession of the magnetization about the external field after the current has subsided. Since the plane of precession is offset from the  $z$  direction due to the in-plane field component, the out-of-plane component of the magnetization oscillates and the period of the oscillations are the same. This is because under this temperature independent model, the anisotropy field is constant and so the oscillation period given by  $2\pi/\gamma H_{ani}$  is constant as well. In reality, the anisotropy field is temperature dependent and so would change due to heating from the current. This effect will be discussed in section 3.3 and 3.4.



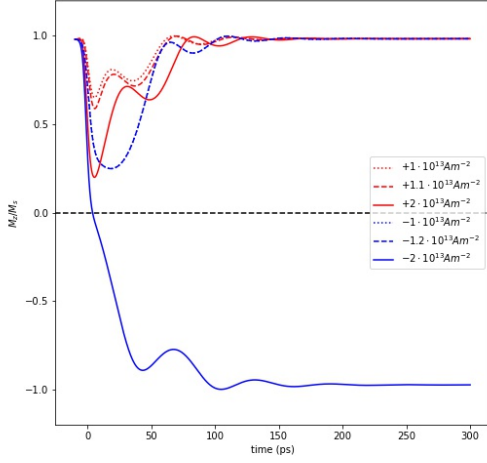
(a) Switching time vs current density curves for various in-plane fields

(b) Critical current density for switching vs in-plane field values

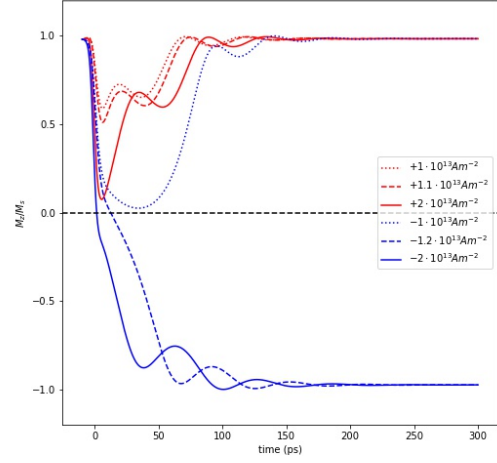
Figure 3.4: (a) shows the dramatic decrease in switching time as injected current density increases. It also demonstrates the effect on switching times of the in-plane field due to reversal torque. (b) shows the seemingly linear relation between critical switching current density and in-plane field.

## 3.2 Effect of Free Parameters on Simulation

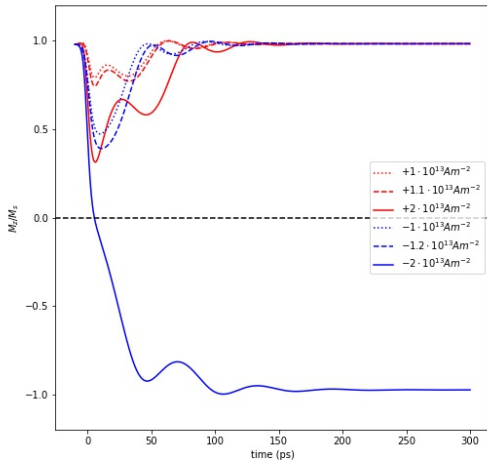
While parameters like the in-plane field, magnetic anisotropy constant, and current density have a major impact on the outcome of the simulation, as was detailed in the previous section, they are system parameters and are derived from the experimental setup. Alternatively, parameters like the spin Hall angles and the Gilbert damping coefficient are empirically determined by fitting the results of the simulation to experimental data. The Gilbert damping parameter was approximated by fitting the number of oscillations, and the delay and length of each oscillation to the experiment's results (see Section 3.4). With this, a surprisingly large  $\alpha \sim 0.23$  was obtained. One explanation for why  $\alpha$  is large may be because it is an empirical fit and so may be accounting for other effects including inhomogeneous broadening [8]. As such,  $\alpha$  behaves more like an effective Gilbert damping parameter. The field-like and damping-like spin Hall angles,  $\theta_{SH}^{FL}$  and  $\theta_{SH}^{DL}$ , were chosen to match values consistent with literature [1]. When investigating the effect of varying the spin Hall angles, the effects were more explicitly identifiable when solving the LLG equation without thermal effects than the case with thermal effects taken into account. The simulation's results for two different values of  $\theta_{SH}^{DL}$  and  $\theta_{SH}^{FL}$  are shown in the figure below:



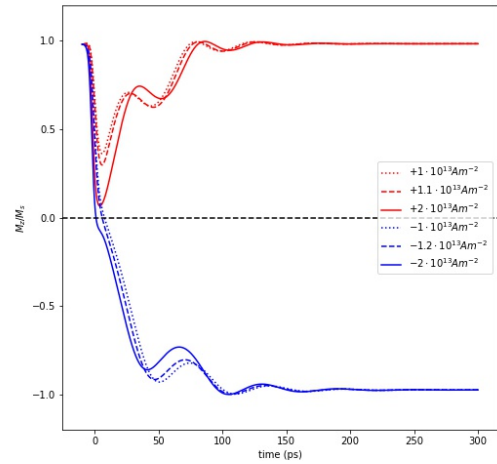
(a) Dynamics of out-of-plane magnetization for a low field-like spin Hall angle,  $\theta_{SH}^{FL} = 0.025$  and  $\theta_{SH}^{DL} = 0.2$



(b) Dynamics of out-of-plane magnetization for a high field-like spin Hall angle,  $\theta_{SH}^{FL} = 0.10$  and  $\theta_{SH}^{DL} = 0.2$



(c) Dynamics of out-of-plane magnetization for a low damping-like spin Hall angle,  $\theta_{SH}^{DL} = 0.23$  and  $\theta_{SH}^{FL} = 0.05$



(d) Dynamics of out-of-plane magnetization for a high damping-like spin Hall angle,  $\theta_{SH}^{DL} = 0.45$  and  $\theta_{SH}^{FL} = 0.05$

Figure 3.5: Simulation results for high and low values of both spin Hall angles for different current densities and spin polarizations

With a higher damping-like spin Hall angle, the spin current torque that counters the damping torque due to external field is amplified. As a result, smaller current densities would be



necessary to reverse magnetization. Similarly, with current densities kept the same while increasing the damping-like spin Hall angle, the switching times become shorter. On the other hand, lower damping-like spin Hall angles reduce the impact of the spin current's damping torque and so higher current densities would be required to switch the magnetization direction, and switching at the relatively low current densities would be accompanied with lengthened switching times. This is clearly visible in Figure 3.5, where at higher spin Hall angle the  $1.1 \times 10^{13} \text{Am}^{-2}$  current switches in nearly half the time as before and the  $1 \times 10^{13} \text{Am}^{-2}$  current switches when it did not previously. Similarly, at lower spin Hall angle the  $2 \times 10^{13} \text{Am}^{-2}$  current switches slightly slower while the  $1.1 \times 10^{13} \text{Am}^{-2}$  no longer switches. Furthermore, the minimum out-of-plane magnetization that the positive currents achieve is significantly lower with higher damping than otherwise. Lastly, the dynamics 50 ps after the current pulse has subsided are approximately the same, which is to be expected.

Unlike the damping-like spin Hall angle which contributes to the spin current's torque that opposes the external field's damping torque, the field-like spin Hall angle creates a torque that opposes the precessional torque due to the external field. This has a similar effect regarding critical switching current densities and switching times as with damping-like torque. A more unique feature that varying  $\theta_{SH}^{FL}$  reveals is that with a lower precessional torque due to greater opposition from the spin current, the stabilization of the magnetization is slightly delayed, whereas with higher precessional torque and weaker opposition from the spin current the stabilization is slightly quickened. Hence, by varying these parameters to achieve intended modifications to the simulation results, the simulation was tuned to be consistent with literature and match experimental data with values in Table 3.1 as the best fit.

### 3.3 Ultrafast Thermal Dynamics

The model used by the simulation so far assumed that the system remained at room temperature at all times, however, this is not a realistic assumption. As the current is injected into the metallic stack, the thin films undergo Joule heating and can have peak temperatures of 440 K for a current density of  $1.1 \times 10^{13} \text{Am}^{-2}$ , much higher than room temperature. System parameters like the anisotropy field constant (and accordingly the anisotropy field), as well as the saturation magnetization are temperature dependent and so change significantly over the course of time. As the spins are injected, the heating alters the effective external field by decreasing  $H_{ani}$  and  $M_s$ . Due to the lower anisotropy field, the  $z$  component of the external field drops and further tilts the axis and plane of precession, creating a thermal anisotropy torque that aids reversal. As a result, the switching times, critical current density, and overall dynamics of switching is noticeably different than if thermal effects are ignored. While the LLG solutions in the previous sections were adequate approximations of the system, the simulation can be more accurate with its predictions if these affects are accounted for.

If the metallic stack is assumed to be symmetric in two dimensions and varied only in

one direction, the temperature response of the metal film can be estimated by solving the one spatial dimension heat-diffusion equation.

$$C \frac{\partial T}{\partial t} = \Lambda \frac{\partial^2 T}{\partial x^2} + q(t) \quad (3.3)$$

Here  $T(x, t)$  is the temperature of the film,  $C$  is the volumetric heat-capacity,  $\Lambda$  is the metals thermal conductivity, and  $q(t)$  is the external power per unit volume generated due to the electric pulse. Assuming Ohmic behavior, volumetric heating due to the current can be estimated using  $q(t) = \rho_e J^2(t)$ , where  $\rho_e = 8.1 \Omega \text{nm}$  is the measured resistivity across the stack and  $J(t)$  is the current density applied [15]. For the bulk of the simulations,  $J(t)$  will be a Gaussian of FWHM 6 ps with peak current density as the same free variable used in the LLG equation. The volumetric heat-capacity of the full metallic stack,  $C = 2.6 \times 10^6 \text{Jm}^{-3}\text{K}^{-1}$ , is approximated by weighted averaging the heat-capacities of each layer. The thermal conductivity of the stack is calculated using the Wiedemann-Franz law  $\Lambda = L_0 T / \rho_e \sim 9, \text{Wm}^{-1}\text{K}^{-1}$ , where  $L_0$  is the Lorenz number. To solve Eq 3.3, now that all the terms have been defined, boundary conditions need to be established. The metal-film-air interface is assumed to follow an adiabatic boundary condition, while a heat-current per unit area  $J_Q$  escapes from the metal-film-substrate interface. The heat current is modulated by interfacial thermal conductance  $G$  between the Ta and  $\text{SiO}_2$ ,

$$J_Q = G \cdot T(x = d) \quad (3.4)$$

where  $d = 16 \text{ nm}$  is thickness of the film.  $G$  typically lies in the range  $100\text{-}300 \text{ MWm}^{-2}\text{K}^{-1}$  for metal-film-oxide interfaces [6][17][10]. The value of  $G \sim 120 \text{ MWm}^{-2}\text{K}^{-1}$  was deduced by fitting the heat equation solution to match the temperature dependent saturation magnetization at different times. The solutions of the heat equation with different interfacial thermal conductances can be seen in Figure 3.6. The values of parameters used to solve the heat-diffusion equation can be found in Table 3.2 [1].

Table 3.2: Heat Equation Parameter Values

Curie Temperature	$T_C$	800	K
Volumetric heat capacity	$C$	$2.6 \times 10^6$	$\text{Jm}^{-3}\text{K}^{-1}$
Interfacial thermal conductance	$G$	$120 \times 10^6$	$\text{Wm}^2\text{K}^{-1}$
Thickness of magnetic layer	$d_0$	1	nm
Thickness of full stack	$d$	16	nm
Thermal conductivity of the metal	$\Lambda(300\text{K})$	9	$\text{Wm}^{-1}\text{K}^{-1}$
Electrical resistivity	$\rho_e$	$81 \times 10^{-8}$	$\Omega\text{m}$
Current density	$J_C$	variable	$\text{Am}^{-2}$

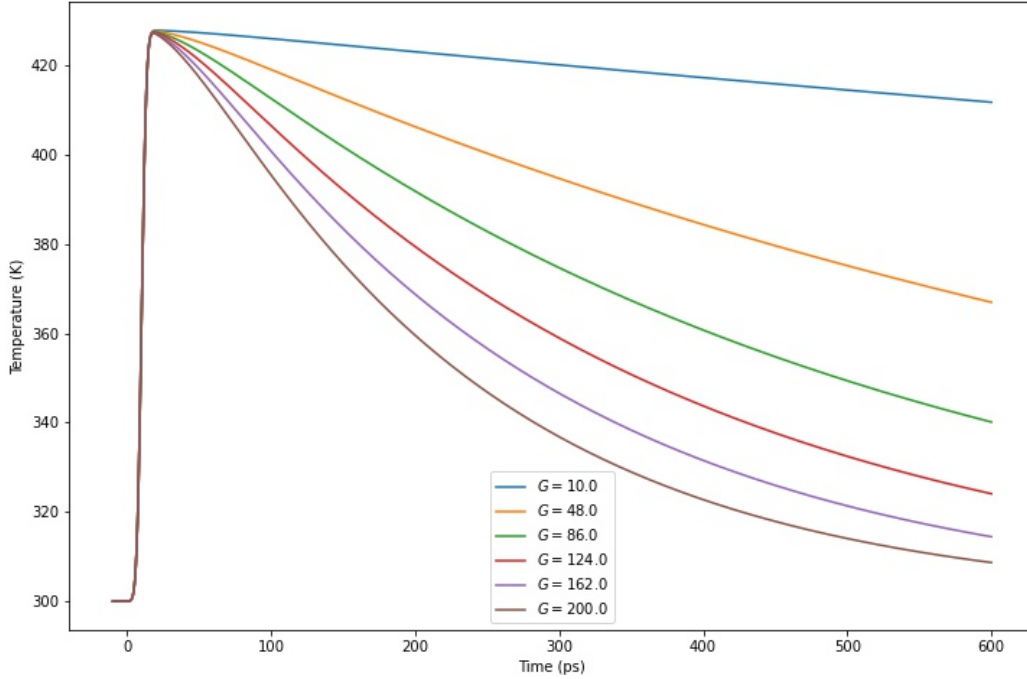


Figure 3.6: Solutions to the heat diffusion equation for different interfacial thermal conductance values. The expected range is  $[100, 200]$   $\text{MWm}^{-2}\text{K}^{-1}$ . The value for the simulation was chosen by matching the saturation magnetization at 600 ps in the experimental data to these results.

While it may be possible to solve the the heat-diffusion partial differential equation analytically for Gaussian current densities using separation of variables and Green's functions, it is sufficient to solve it numerically using the finite differences method in which temperature was evolved forward in time using 1 fs steps. It was once again verified that the solution remained stable and unchanged at smaller step sizes.

## Finite Difference Method

The finite differences method utilizes the Taylor series to approximate higher order derivatives of a function  $f(x)$  while also providing some measure of error in approximation.

$$f(x + \Delta x) = f(x) + \Delta x f'(x) + \frac{\Delta x^2}{2!} f''(x) + \frac{\Delta x^3}{3!} f^{(3)}(x) + \frac{\Delta x^4}{4!} f^{(4)}(x) + \dots \quad (3.5)$$

Rearranging the terms, dividing by  $\Delta x$ , and taking the limit  $\Delta x \rightarrow 0$ ,

$$\frac{f(x + \Delta x) - f(x)}{\Delta x} = f'(x) + O(\Delta x) \quad (3.6)$$

where  $O(\Delta x)$  suggests that error in approximating the first derivative grows linearly with the step size. Considering the same procedure for  $f(x - \Delta x)$ ,

$$f(x - \Delta x) = f(x) - \Delta x f'(x) + \frac{\Delta x^2}{2!} f''(x) - \frac{\Delta x^3}{3!} f^{(3)}(x) + \frac{\Delta x^4}{4!} f^{(4)}(x) - \dots \quad (3.7)$$

and subtracting it from Eq. 3.5, once again taking the limit, another approximation called the central approximation for obvious reasons can be deduced:

$$\frac{f(x + \Delta x) - f(x - \Delta x)}{2\Delta x} = f'(x) + O(\Delta x^2)$$

The central approximation error dies quadratically and so would converge to the derivative much faster than the forward difference equation. However, since the first derivative of importance in the case of the heat-diffusion equation is time and the system is causal, only the forward difference equation can be used. The comparison between the two approximations is meaningful, nonetheless, as it is informative about the step sizes required and the impact on accuracy of step sizes that are too large. Furthermore, since the spatial derivatives are not spatially causal, this comparison also reveals that the central second derivative approximation would be optimal and would not require small step sizes to converge. Adding Eq 3.5 and 3.7, rearranging the terms, dividing by  $\Delta x^2$  and taking the limit as the step size goes to 0,

$$\frac{f(x + \Delta x) - 2f(x) + f(x - \Delta x)}{\Delta x^2} = f''(x) + O(\Delta x^2) \quad (3.8)$$

Finally, the time evolution relation for the heat-diffusion equation can be determined.

$$T(t + \Delta t, x) = \frac{\Lambda}{C} \frac{\Delta t}{\Delta x^2} (T(t, x + \Delta x) - 2T(t, x) + T(t, x - \Delta x)) + \frac{1}{C} q(t) + T(t, x) \quad (3.9)$$

When solving the heat-diffusion equation using the approximation in Eq 3.9, as mentioned previously  $\Delta t = 1$  fs and  $\Delta x = 16$  pm (i.e. 1000 divisions) were used. In addition to the expression above, the boundary conditions need to also be expressed with finite difference. The adiabatic condition at the film-surface interface implies that the heat flux at the surface is 0, i.e.  $\partial T / \partial x = 0$  at  $x = 0$ . The forward difference equation 3.5 with a 0 derivative suggests that  $T(x + \Delta x) = T(x - \Delta x)$ , where of course  $x - \Delta x$  is outside of the film but this expression can be used to get time evolution of temperature at the surface using the second spatial derivative,

$$\left. \frac{\partial^2 T}{\partial x^2} \right|_{x=0} = \frac{2T(t, x + \Delta x) - 2T(t, x)}{\Delta x^2} \quad (3.10)$$

The heat-current escaping from the bottom of the film to the substrate leaks energy at a rate of

$$\frac{\partial Q}{\partial t} = -GT(x=d)A = CA d \frac{\partial T}{\partial t} \Big|_{x=d} \quad (3.11)$$

where  $A$  is the area of the cross section. After deriving the temperature derivative due to the heat current and combining it with thermal heating from the current, the final expression for the second boundary condition is

$$\frac{\partial T}{\partial t} \Big|_{x=d} = -\frac{G}{Cd}T(x=d) + \frac{1}{C}q(t) \quad (3.12)$$

The heat-diffusion equation was solved using this outlined method and results for different interfacial thermal conductance values can be found in Figure 3.6. Since the solution will be a function of depth and only the temperature of Co is relevant to the simulation, the temperature used is the average temperature over the range of  $x$  that corresponds with the depth and thickness of the Co layer. An important point to note here is that by using a one-temperature model, the electron, spins, and phonons are assumed to be thermal equilibrium. While on picosecond timescales non-equilibrium between the thermal reservoirs of the three systems can occur and drive ultrafast magnetic phenomena, for pulses longer than a few picoseconds and with strong thermal coupling between the phonons and electrons in Co, the non-equilibrium is expected to be small [16]. Hence, the one-temperature model used above is an adequate approximation.

## Effect of Ultrafast Heating on SOT Simulation

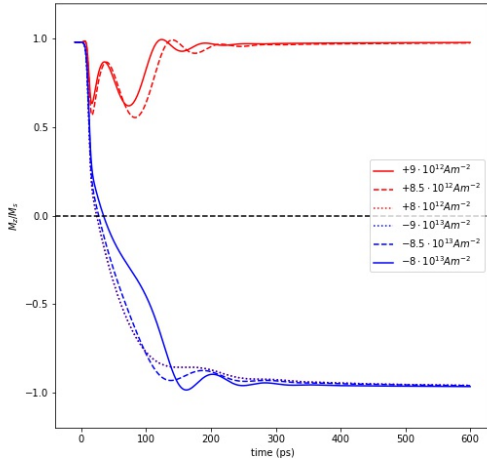
As aforementioned, the saturation magnetization and the anisotropy field are both temperature dependent [9]. In addition to the thermal anisotropy torque explained at the beginning of the section, the drop in the  $z$  component simply due to ultrafast heating even in the absence of injected spins causes the effective external field to tilt further in the  $x$  direction and induces precessional dynamics [2]. To simulate the effects of ultrafast heating on SOT driven switching, the saturation magnetization and anisotropy field are allowed to be functions of time and the LLG equation is solved accordingly. The two components are made functions of time by first defining them as functions of temperature and then combining these relations with the temperature solution to the heat-diffusion equation from the previous section. Following Ref [9], the magnetization and magnetocrystalline anisotropy is assumed to be described by

$$M_s(T) = M_s(0)[1 - (T/T_C)^{1.7}] \quad (3.13)$$

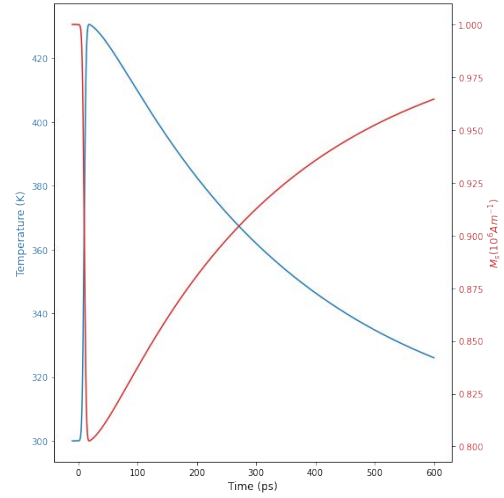
$$K_z(T) = K_z(0)[M_s(T)/M_s(0)]^3 \quad (3.14)$$

where  $T_C$  is the Curie temperature of Co,  $M_s(0)$  is the saturation magnetization at absolute zero, and  $K_z(0)$  is anisotropy constant at absolute zero. The value of  $M_s(T = 300K)$  is fixed to  $10^6 \text{ Am}^{-1}$  from VSM measurements and the value of  $M_s(0)$  is calculated using Eq

3.13. The anisotropy constant at room temperature  $K_z(T = 300K)$  was fit to  $10^6 \text{ Jm}^{-3}$  by measuring the corresponding out-of-plane anisotropy field. For more details about how the anisotropy constant was estimated see Ref [1]. The results of the simulation with temperature dynamics taken into consideration can be seen in Figure 3.7 below.



(a) SOT driven switching dynamics with ultrafast heating



(b) Solution to the heat diffusion equation used by the model for  $J_C = 8 \times 10^{12} \text{ Am}^{-2}$  and the resulting saturation magnetization over time

Figure 3.7: Dynamics of the out-of-plane magnetization as predicted by the LLG model with thermal effects taken into consideration.

As can be seen in the above plot, with thermal effects taken into account, the critical switching current decreased from  $1.1 \times 10^{13} \text{ Am}^{-2}$  to  $8 \times 10^{12} \text{ Am}^{-2}$  with a switching time of  $\sim 30$  ps. For currents greater than the critical switching current, the switching time once again dramatically decreases. For both positive and negative currents, the out-of-plane magnetization reaches 80% of saturation magnetization between 50 - 150 ps depending on the current density. It is important to note that saturation magnetization depends only on the ratio of current temperature to the material's Curie temperature ( $T_C = 800 \text{ K}$  for Co). As a result, even at temperatures 60 K above room temperature the saturation magnetization recovers to around 85%. It appears that the more noticeable effect of thermal heating on the simulation is the decreased critical switching current density due to thermal anisotropy torque. It is difficult to compare observations about demagnetization time and zero crossing time to the predictions of the LLG model without ultrafast heating. Nonetheless, at currents near or at the critical switching current density, the LLG model with ultrafast heating takes longer to

reach 80% magnetization and stabilize than the model without ultrafast heating. Another interesting feature of the results in Figure 3.7 is that for positive currents the two large dips in out-of-plane magnetization due to precession have different durations. This is due to the lower value of  $H_{ani}$  as temperature rises because of which the period of oscillation  $2\pi/\gamma H_{ani}$  increases. Of course, this feature could not be predicted without incorporating temperature dynamics. Since the pulse width and overall current distribution remains unchanged between the two LLG models, it is clear that the ultrafast heating and the precessional dynamics it induces are a significant contributor to the switching mechanism. Furthermore, the lower switching currents with ultrafast heating suggests that the energy density required to switch the thin film, or in the context of data storage the write energy, is accordingly smaller than what the previous model estimates.

### 3.4 Comparing Simulation to Experimental Data

The validity of the simulation was tested by comparing its predictions to experimental data of the same metallic stack with 1 nm Co magnetic thin film. The experimental setup used to generate the picosecond electrical pulses as well as to detect magneto-optical phenomena is shown in Figure 3.8 below.

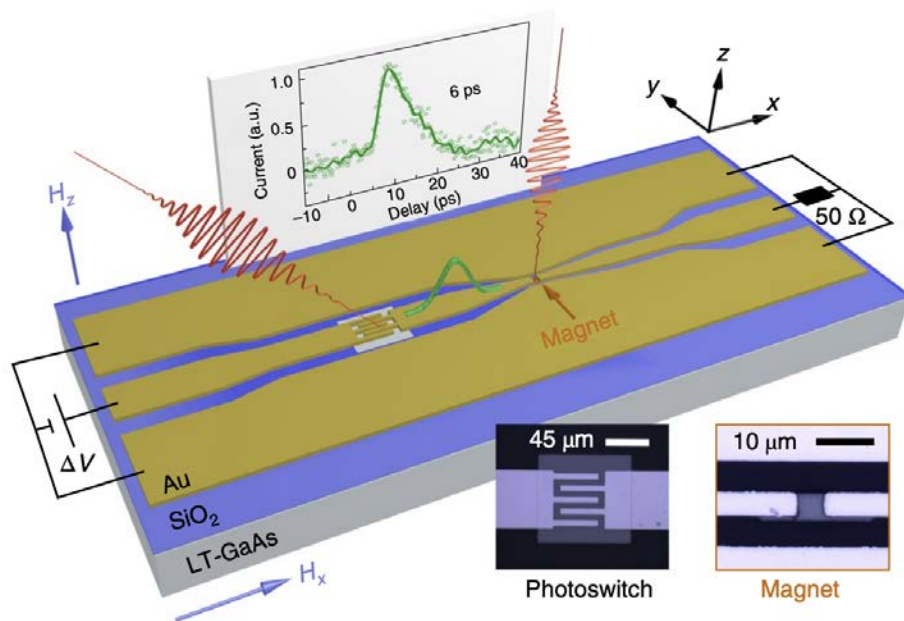


Figure 3.8: The photoswitch is irradiated by an optical pump and creates a picosecond electrical pulse which can be seen in the green curve.

The approximately 6 picosecond electrical pulse was generated by exciting the photoconductive switch in Figure 3.8 with an optical pump. Both the left and right side of the transmission line were contacted with a CPW 40 GHz GGB probe tip along with a  $50 \Omega$  resistor to complete the circuit. The leakage current when there was no optical excitement due to finite switch resistance was measured by applying a constant voltage bias between -50 V to 50 V to the left contact. The switch was then irradiated with either a  $0.3 \mu\text{J}$  pulse from a 5 kHz laser or  $0.37 \text{ nJ}$  pulse from an 80 MHz oscillator system. The current generated by the photoswitch was then fine tuned by adjusting the pump mirror. The final switching state was measured with MOKE micrographs using an in-house made MOKE microscope. Further details about time resolved dynamics measurements and pulse generation can be found in Ref [1]. The plot of the experimental data of time-resolved magnetization superimposed with the simulation predictions can be found below.

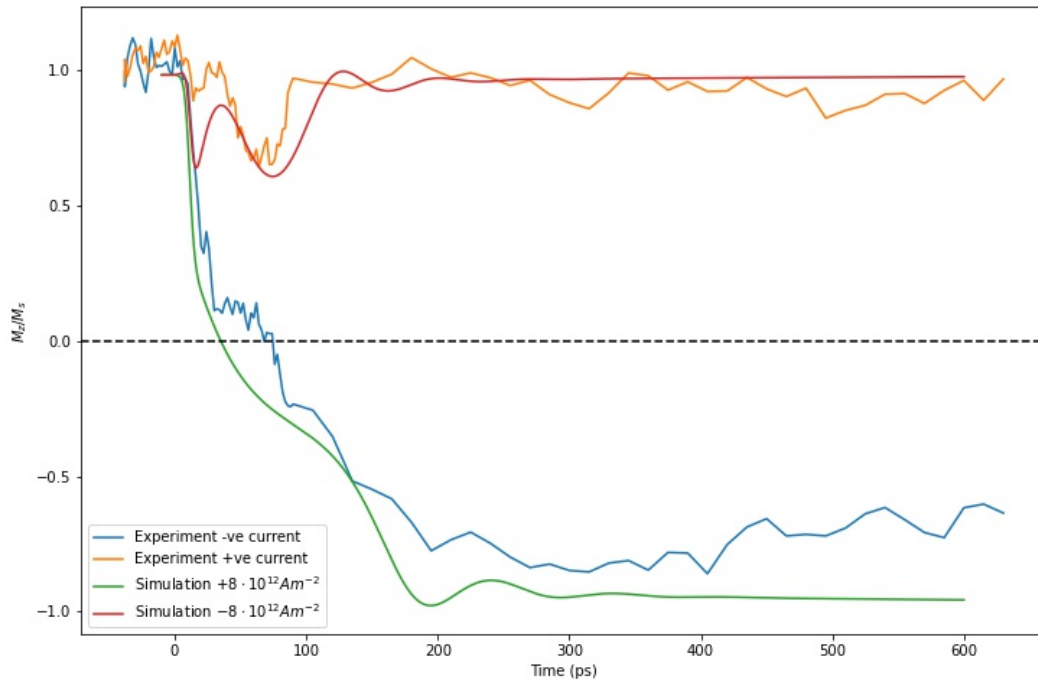


Figure 3.9: Dynamics predicted by the modified LLG model superimposed with experimental results for comparison.

The above plot shows that the simulation matches the general dynamics of the experiment well. In particular, the positive current predictions represented by the red curve follows the experimental data very well. The delay and width of the oscillations in magnetization



due to precession of the actual and predicted data match. Both show demagnetization for approximately 120 ps, and stabilization around 150 ps in the positive current case. Furthermore, the prediction that 80% of remagnetization will be achieved around 150 ps in the case of positive current is validated by the experiment. The negative current dynamics also both stabilize around 200 ps. The simulation for negative current follows the experimental results closely but switches and remagnetizes faster. The predicted switching time is  $\sim 35$  ps while the experiment's switching time is around 60 ps (note that the electrical pulse in the plot peaks at approximately 30 ps). The simulation evidently demagnetizes much faster than the actual data. The out-of-plane magnetization in the experiment, represented as the yellow curve for positive current and blue for negative current, never fully remagnetize in the 600 ps time scale. Both curves reach approximately 85% of saturation magnetization while the simulation predicts that the out-of-plane magnetization will come very close to remagnetizing. One key difference between the simulation and the experiment that may explain this disagreement is that the experiment exhibits an additional precession right before zero crossing while the simulation does not predict any such behavior. This results with zero crossing being slightly delayed relative to that of the simulation. At this moment, it is difficult to understand why the simulation does not predict this precession. It may be due to an additional torque and would require further investigation. It is also important to note that since many of the parameters were fit and the exact temperature dependence of  $M_s$  and  $K_z$  is unknown for temperatures much higher than room temperature, the simulation is not entirely representative of the metallic stack.

As was previously mentioned, the predicted critical switching current is  $\approx 8 \times 10^{12} \text{Am}^{-2}$  whereas the actual threshold is in the range  $[6 \times 10^{12}, 7 \times 10^{12}] \text{Am}^{-2}$ . The actual threshold value varies in that range due to variance in the pulse width. With large uncertainty in the experiment and with the fit values used in the simulation, the model seems to be in excellent agreement with the experimental data. That said, one explanation for the difference between the two critical switching current values is that the simulation assumes that the current passes through the entire metallic stack. In reality, the 1 nm thickness of Co causes the layer to have high resistivity relative to Pt and Ta and so majority of the current goes through the Pt and Ta layers. As a result, the current density through the Pt and Ta layers increases along with the spins injected into the Co. As such, a smaller current density across the cross section would be required reverse the magnetization of Co. Nonetheless, the simulation is a good approximation of the true dynamics of the metallic stack and is useful to identifying and predicting trends with ease.

## Chapter 4

# Conclusion and Future Works

In this work, the Landau-Lifshitz-Gilbert macrospin model for a ferromagnetic thin film of Co in the presence of an external magnetic field was extended to include the effect of injected spins due to the spin Hall effect from Ta and Pt layers. The behavior of the magnetic stack when different current densities and spin polarizations were passed through was simulated and conditions for magnetization reversal were noted. In particular, it was demonstrated that switching time decreased drastically as current density increased: for instance, with an in-plane field of 150 mT, the switching time at threshold current density and 150% threshold current density was around 25 ps and 5 ps, respectively. Furthermore, the relationship between critical current density for switching and in-plane field was explored and it was revealed that the critical current density decreased linearly with increasing in-plane field values.

The ultrafast thermal effects of Joule heating from the current on the magnetization dynamics was incorporated by first solving the heat diffusion equation of the metallic stack and modeling the variations in saturation magnetization and anisotropy constant as functions of temperature. Comparing the modified simulation results with experimental data showed that, in the case of a positive current, the simulation followed the dynamics of the experiment very well and matched precession and demagnetization scales. In the case of negative currents, the simulation demagnetized at a faster rate and so switched faster. Nonetheless, the results followed the experiment closely and demonstrated switching at and stabilization at timescales shorter than 200 ps. Another notable distinction between the simulation and the experimental data was that the predicted critical switching current with an in-plane field of 150 mT is  $8 \times 10^{12} \text{ Am}^{-2}$  while the actual critical switching current was expected to be in  $[6 \times 10^{12}, 7 \times 10^{12}] \text{ Am}^{-2}$ . However, with large uncertainty in the experiment data and in the fits used by the simulation, the predicted results are in excellent agreement with the experiment. Nonetheless, the model makes simplifying assumptions that can be made more realistic. The simulation assumes that the current passes through all layers equally, and that system parameters like resistivity and the Lorenz number remain unchanged at higher temperatures. These assumptions are not true at temperatures much higher than room temperature as resistivity scales with temperature (and thickness as well), and the current

density through each layer is a function of the resistivity of that layer. Hence, in the future more modifications can be made to the simulation to make it more accurate. For instance, a non-uniform spatial current density distribution based on resistivity of layers can be used when solving the heat diffusion and when determining the spin current torques. With all of these modifications, the SOT driven switching simulation can be used to simulate any metallic stack with a magnetic thin film to identify critical switching current densities, switching and demagnetization times, and power consumption for different setups, thus informing the engineering of magnetic memory without the direct need for experiments as a first step.

## References

- [1] Kaushalya Jhuria et al. “Spin–orbit torque switching of a ferromagnet with picosecond electrical pulses”. In: *Nature Electronics* 3 (Nov. 2020), pp. 680–686. DOI: 10.1038/s41928-020-00488-3.
- [2] U. Atxitia et al. “Micromagnetic modeling of laser-induced magnetization dynamics using the Landau-Lifshitz-Bloch equation”. In: *Applied Physics Letters* 91.23 (2007), p. 232507. DOI: 10.1063/1.2822807.
- [3] Debanjan Bhowmik et al. “Magnetization Switching and Domain Wall Motion Due to Spin Orbit Torque”. In: *Nanomagnetic and Spintronic Devices for Energy-Efficient Memory and Computing*. John Wiley and Sons, Ltd, 2016. Chap. 6, pp. 165–187. ISBN: 9781118869239. DOI: <https://doi.org/10.1002/9781118869239.ch6>.
- [4] J. M. D. Coey. *Magnetism and Magnetic Materials*. 2009, p. 633.
- [5] Kevin Garello et al. “Ultrafast magnetization switching by spin-orbit torques”. In: *Applied Physics Letters* 105.21 (2014), p. 212402. DOI: 10.1063/1.4902443.
- [6] Patrick E. Hopkins. “Thermal Transport across Solid Interfaces with Nanoscale Imperfections: Effects of Roughness, Disorder, Dislocations, and Bonding on Thermal Boundary Conductance”. In: *International Scholarly Research Notices* 2013 (2013), pp. 1–19.
- [7] M. Lakshmanan. “The fascinating world of the Landau-Lifshitz-Gilbert equation: an overview”. In: *Philosophical Transactions: Mathematical, Physical and Engineering Sciences* 369.1939 (2011), pp. 1280–1300. ISSN: 1364503X.
- [8] Dustin M. Lattery et al. “Quantitative analysis and optimization of magnetization precession initiated by ultrafast optical pulses”. In: *Applied Physics Letters* 113.16 (2018), p. 162405. DOI: 10.1063/1.5046683.
- [9] Kyoung-Min Lee et al. “Temperature dependence of the interfacial magnetic anisotropy in W/CoFeB/MgO”. In: *AIP Advances* 7.6 (2017), p. 065107. DOI: 10.1063/1.4985720.
- [10] Christian Monachon, Ludger Weber, and Chris Dames. “Thermal Boundary Conductance: A Materials Science Perspective”. In: *Annual Review of Materials Research* 46.1 (2016), pp. 433–463. DOI: 10.1146/annurev-matsci-070115-031719.

- [11] Dmitri E. Nikonov and Ian A. Young. “Overview of Beyond-CMOS Devices and a Uniform Methodology for Their Benchmarking”. In: *Proceedings of the IEEE* 101.12 (2013), pp. 2498–2533. DOI: 10.1109/JPROC.2013.2252317.
- [12] Akshay Pattabi. “Investigation and Control of Ultrafast Magnetic Phenomena”. PhD thesis. EECS Department, University of California, Berkeley, Aug. 2020. URL: <http://www2.eecs.berkeley.edu/Pubs/TechRpts/2020/EECS-2020-176.html>.
- [13] D.C. Ralph and M.D. Stiles. “Spin transfer torques”. In: *Journal of Magnetism and Magnetic Materials* 320.7 (2008), pp. 1190–1216. ISSN: 0304-8853. DOI: <https://doi.org/10.1016/j.jmmm.2007.12.019>.
- [14] H. Sato et al. “14ns write speed 128Mb density Embedded STT-MRAM with endurance  $10^{10}$  and 10 yrs retention  $85^{\circ}\text{C}$  using novel low damage MTJ integration process”. In: *2018 IEEE International Electron Devices Meeting (IEDM)* (2018), pp. 27.2.1–27.2.4.
- [15] Y. S. Touloukian. “Recommended Values of the Thermophysical Properties of Eight Alloys, Major Constituents and their Oxides Thermophysical Properties Research Center”. In: *Purdue University* (1966).
- [16] Matthieu J. Verstraete. “Ab initio calculation of spin-dependent electron-phonon coupling in iron and cobalt.” In: *Journal of physics. Condensed matter : an Institute of Physics journal* 25 13 (2013), p. 136001.
- [17] R. B. Wilson et al. “Thermal conductance of strongly bonded metal-oxide interfaces”. In: *Phys. Rev. B* 91 (11 Mar. 2015), p. 115414. DOI: 10.1103/PhysRevB.91.115414.
- [18] Seonghoon Woo et al. “Enhanced spin-orbit torques in Pt/Co/Ta heterostructures”. In: *Applied Physics Letters* 105.21 (2014), p. 212404. DOI: 10.1063/1.4902529.